九州大学学術情報リポジトリ
Kyushu University Institutional Repository

Numerical prediction of cavitation in centrifugal pump using Multi-Process cavitation model

YAMADA, Akihisa
Graduate School of Engineering, Kyushu University

INO, Takeshi
Graduate School of Engineering, Kyushu University

TSUDA, Shin-ichi
Department of Mechanical Engineering, Kyushu University

WATANABE, Satoshi
Department of Mechanical Engineering, Kyushu University

他

https://hdl.handle.net/2324/7357482

出版情報：Journal of Fluid Science and Technology. 19 (2), pp.JFST0011-JFST0011, 2024. 日本機械学会
バージョン：
権利関係：Creative Commons Attribution 4.0 International

KYUSHU UNIVERSITY

Bulletin of the JSME
Vol.19, No.2, 2024
Journal of Fluid Science and Technology

Numerical prediction of cavitation in centrifugal pump using Multi-Process cavitation model

Akihisa YAMADA*, Takeshi INO*, Shin-ichi TSUDA**, Satoshi WATANABE**
and Taiki TAKAMINE***
*Graduate School of Engineering, Kyushu University
744 Motooka, Nishi-ku, Fukuoka, 819-0395, Japan
E-mail: yamada.akihisa.679@s.kyushu-u.ac.jp
**Department of Mechanical Engineering, Kyushu University
744 Motooka, Nishi-ku, Fukuoka, 819-0395, Japan
***Department of Mechanical Engineering, Kobe City College of Technology
8-3, Gakuen-Higashimachi, Nishi-ku, Kobe, 651-2194, Japan

Received: 19 October 2023; Revised: 16 November 2023; Accepted: 15 December 2023

Abstract
In the present study, numerical simulation of cavitating flow using Multi-Process model, which is one of the homogeneous cavitation models and consists of multiple transport equations of bubbly flow characteristics defined on the basis of the moment method, is conducted for a centrifugal pump toward more accurate prediction. The experiment is also conducted for the same pump to obtain the hydraulic performance including the axial thrust force characteristics as well as the visual aspects of cavitation for the validation of numerical simulation. It is found that the present simulation can qualitatively reproduce the degradation of pump suction performance as well as the change in axial thrust force under cavitation at the design flow rate; thrust forces acting on the impeller and the balance drum decreases with the head drop. The cavity patterns leading to the head drop are also well reproduced; the cavitation on the suction surface extends into the blade passage. At a partial flow rate close to the design one, the simulated cavity patterns with the inception and moderate states of cavitation agree with the observation, but they are not well reproduced perhaps due to the insufficient mesh resolution at the deep partial flow rate where the most of cavitation occurs in the vortical structure, typically in the tip separation vortex.

Keywords : Multi-Process model, Centrifugal pump, Numerical study, Cavitation, Visualization

1. Introduction

Recently, fluid machinery has been required to be multi-stage and high-speed due to the demand for space saving with high pressure. Therefore, the importance of fluid forces acting on the axial system is apparent. Furthermore, the effects of cavitation are expected to be more pronounced in hydraulic machinery with higher rotational speeds, in addition to the increased complexity of internal flow due to multi-stage systems. Cavitation in fluid machines can cause several problems such as degradation of performance, serious damage to materials, and so on. Thus, the development of prediction method of cavitation flow is becoming more important, and numerical and experimental investigations have been conducted. In particular, zero- and one-equation homogeneous media models, with which the computational cost is the lowest, have been implemented in many commercial CFD solvers. A barotropic model that expresses the mixture density of the gas and liquid phases by a function of only pressure is a typical zero-equation model. As an example, Coutier-Delgosha et al. (2003) used Tait equation of state (EOS) for liquid and ideal gas EOS for vapor to establish a function that defines the relationship between pressure and density. One-equation homogeneous models are more commonly employed in commercial software. Schnerr and Sauer (2002) proposed a one-equation homogeneous model (hereafter called SS model) derived from the assumption of dilute bubbly flows of constant bubble number density, in which a simplified Rayleigh–Plesset equation is employed to relate the bubble radius change with the local pressure. Zwart-Gerber-Belamri (ZGB) cavitation model also employs the simplified Rayleigh equation, but it considers the different bubble surface densities between the evaporation and condensation states (Zwart et al., 2004). So-called Full Cavitation (FC) model was developed by Singhal et al. (2002), which considers the effects of turbulence and non-

Paper No.23-00452
[DOI: 10.1299/jfst.2024jfst0011]
© 2024 The Japan Society of Mechanical Engineers. This is an open access article under the terms of the Creative Commons Attribution 4.0 International license (https://creativecommons.org/licenses/by/4.0/).

condensable gases with the framework of one-equation model. These one-equation models are often used for the simulation of turbomachines because the internal geometry is complex and the number of required meshes is generally large. Medvitz et al. (2002) simulated a centrifugal pump with a seven-blade impeller across a wide range of flow rates and discussed cavitation phenomena including head reduction while comparing with experiments. Nohmi et al. (2003) also conducted experiments and analyses for a low specific speed pump and reported that breakdown characteristics can be predicted by a homogeneous media model at the best efficiency point. However, the deviations from the experiment were observed at a high flow rate due to inadequate inlet boundary conditions. Miyabe et al. (2011) predicted the cavitation erosion in a double suction centrifugal pump by utilizing the erosion prediction index proposed by Nohmi et al (2009). Sun and Tan (2020) performed the cavitation analysis of a centrifugal pump at a partial flow rate condition using the modified ZGB model, focusing on pressure fluctuations due to cavitation-vortex. However, the breakdown characteristics under partial flow rate were not estimated accurately. Karakas et al. (2022) recently conducted cavitation simulations of a pump with an inducer with four cavitation models. They reported that ZGB and SS model were suitable for their application by considering the computation time, the convergence level and the qualitative agreement with the measured data. Although these reports presented the qualitative agreements in their analyses, the prediction accuracy of the homogeneous media model is still insufficient. Recently, Multi-Process (MP) model has been developed by Tsuda and Watanabe (2015), that is a homogeneous model which can take account of the main elementary processes in cavitation bubbles, i.e., inception/collapse, evaporation/condensation, growth/shrinkage and coalescence/break-up using the moment method (Randolph, 1971) for a size distribution function of cavitation bubbles. It solves some equations for moment variables corresponding to the densities of the number of bubbles, the bubble radius, the bubble surface, and the bubble volume. Therefore, it is expected to improve the prediction accuracy, compared to typical one-equation models which only consider the time development of the void fraction driven by expansion/shrinkage. The model has been validated for a simple geometry such as a hydrofoil by Tsuda and Watanabe (2015) showing some potential to increase the prediction accuracy of cavitating flows, and it has been implemented in a commercial CFD solver (Miki et al., 2021); however, it has not yet been applied for complex fluid machinery.

In this study, unsteady RANS (Reynolds Averaged Navier-Stokes) simulation using MP model was carried out for the final stage model of a three-stage centrifugal pump used in our experimental studies (Takamine et al., 2018; Takamine et al., 2020). The results of suction performance, torque, and shaft thrust obtained from the analysis were compared with experimental results to clarify the mechanism of the head reduction, shaft power, and shaft thrust variation of this target pump.

2. Methods

2.1 Target pump

Figure 1 shows a schematic view of the final stage model of the three-stage centrifugal pump used as a target pump in this study. Although it is obvious that cavitation occurs mainly in the first stage of a multi-stage centrifugal pump, the final stage model was selected for the visualization experiments. Specifications of this pump model are summarized in Table 1 (Takamine et al., 2018; Takamine et al., 2020).

Table 1 Specifications of target pump

Design specification	
Rotational speed, N [min^{-1}]	1600
Flow rate, Q_d [m^3/min]	1.5
Head, H_d [m]	38
Specific speed, n [m, m^3/min, min^{-1}]	128
Impeller	
Number of blades	7
Outer diameter, D_2 [mm]	318
Diffuser	
Number of vanes	10
Inlet diameter, D_3 [mm]	325.5

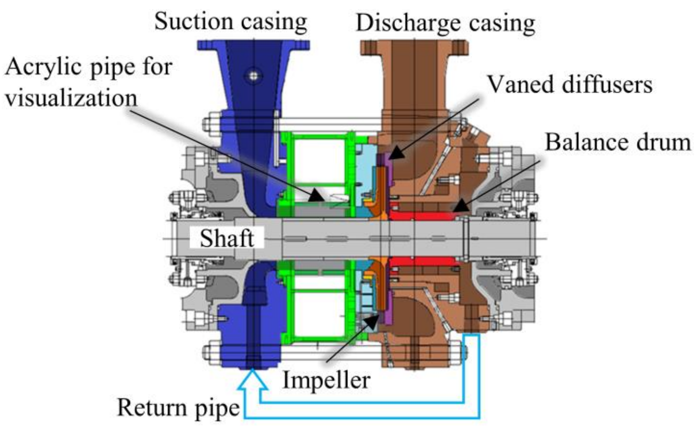

Fig. 1 Final stage model of three-stage centrifugal pump

 © 2024 The Japan Society of Mechanical Engineers

2.2 Multi-Process cavitation model

In homogeneous flow approach of cavitating flow, mass and momentum conservation laws as fundamental equations are employed for the liquid-vapor mixture media whose density ρ is expressed using the volume fraction of vapor, i.e., void fraction α, as follows,

$$\rho = \rho_{\mathrm{L}}(1-\alpha) + \rho_{\mathrm{V}}\alpha \tag{1}$$

where ρ_{L} and ρ_{V} are the densities of liquid and vapor phases respectively. Then, mass and momentum conservation equations in Reynolds-averaged form are;

$$\frac{\partial \rho}{\partial t} + \frac{\partial \rho u_i}{\partial x_i} = 0 \tag{2}$$

$$\frac{\partial \rho u_i}{\partial t} + \frac{\partial \rho u_i u_j}{\partial x_j} = \frac{\partial \tau_{ij}}{\partial x_j} - \frac{\partial P}{\partial x_i} \tag{3}$$

where t is the time, x_i is the position coordinate, P is the pressure, u_i is the flow velocity vector and τ_{ij} is the share stress tensor, in which i or j denotes each space direction.

As one of the homogeneous cavitation models considered to determine the void fraction more precisely, MP model has been constructed on the basis of the moment method (Tsuda and Watanabe, 2015). In this method, "i-th moment M_i" is defined using the size distribution function $f(R)$ below,

$$M_i = \int_0^{\infty} R^i f(R,t) dR \tag{4}$$

$$\frac{DM_i}{Dt} = iGM_{i-1} + R_{\mathrm{c}}^i J_{\mathrm{s}} \quad (\text{for } i = 0,1,2,3\ ) \tag{5}$$

$$G = \frac{DR}{Dt} = C_{\mathrm{g}}\mathrm{sgn}(P_{\mathrm{v}} - P)\sqrt{\frac{2}{3}\frac{|P_{\mathrm{V}}-P|}{\rho_{\mathrm{L}}}} \tag{6}$$

$$J_{\mathrm{s}} = f_0(R_{\mathrm{c}})G \tag{7}$$

where R is the bubble radius, M_0 is the bubble number density [1/m^3], M_1 is the bubble radius density [m/m^3], M_2 is the bubble surface density [m^2/m^3], and M_3 is the bubble volume density [m^3/m^3]. Equation (5) is derived from Eq. (4) as the differential equation in the flow field. In this study, the four equations in Eq. (5) are solved for cavitation coupling with the continuity and momentum equation of homogeneous liquid-vapor mixture Eqs. (2) and (3). A feature of MP model is that R.H.S. in Eq. (5) can reflect various elementary processes of cavitation bubbles such as inception/collapse, expansion/shrinkage, and coalescence/breakup. G in Eq. (6) is the growth rate of bubble radius DR/Dt, and it has been modeled by the typical simplified Rayleigh-Plesset equation for a single spherical bubble. C_{g} is a model coefficient. This constant can be set to different values for the expansion/shrinkage process separately, such as C_{e} and C_{s}. Furthermore, in Eq. (7), G is also applied to the calculation of inception rate, J_{s}, and J_{s} is estimated by the product of G and $f_0(R_{\mathrm{c}})$ given by a size distribution function for preexisting bubble nuclei proposed by Wang (1999), where R_{c} is a certain threshold size. Here, $f_0(R_{\mathrm{c}})$ was regarded as a constant value; 3.88×10^9 m^{-4} is given from the solver default setting determined according to the original paper (Wang, 1999). Void fraction α and the quality Y in the MP model are calculated using M_3 by Eqs. (8) and (9), respectively.

$$\alpha = \frac{\frac{4}{3}\pi M_3}{1 + \frac{4}{3}\pi M_3} \tag{8}$$

$$Y = \frac{\rho_{\mathrm{V}}\frac{4}{3}\pi M_3}{\rho_{\mathrm{L}} + \rho_{\mathrm{V}}\frac{4}{3}\pi M_3} \tag{9}$$

© 2024 The Japan Society of Mechanical Engineers

In the original paper (Tsuda and Watanabe, 2015), Eq. (5) also took account of the coalescence/break-up of bubbles, and the surface tension term was considered in the simplified Rayleigh-Plesset equation, whose growth rate depends on the mean radius of the bubbles. However, these two factors are neglected for simplicity in this study.

2.3 Numerical method

For the CFD simulations, a commercial code, scFLOW, that is an FVM (finite volume method) solver developed by Hexagon, is used. Figure 2 shows a sectional view of the computation domain. The numerical model contains all the flow channels of the target pump including the leakage flow passages in the front and back sides of the impeller and the balancing channel as well as the main flow channels of the impeller, the diffuser and the volute. The model is composed of hexahedral meshes except for the volute domain where tetra-prism meshes are employed. The number of computational elements is totally about 18 million. For the turbulent closure of RANS simulation, the shear-stress transport k-ω model is applied. The compressibility of homogeneous medium is considered by EOS that combines the ideal gas EOS for vapor phase with Tammann EOS for liquid phase as similar to Saito et al. (2003). The mixture density is defined as follows, and it is used instead of Eq. (1);

$$\rho = \frac{P(P+P_{\mathrm{c}})}{K(1-Y)P(\Theta+\Theta_0)+R_{\mathrm{v}}Y(P+P_{\mathrm{c}})\Theta} \tag{10}$$

where R_{v} is the gas constant of water vapor, K is the liquid constant, P_{c} and Θ_0 are the pressure and absolute temperature constants. These values are set at the defaults in the solver. Assuming that water cavitation at normal temperature is an isothermal process, absolute temperature Θ is set at the constant value of 293 K. Note that, in Eq. (9), ρ_{V} is given as the constant value under the saturated vapor pressure at this temperature while ρ_{L} is given by substituting the pressure P and $Y=0$ into Eq. (10).

For the inlet and outlet boundary conditions, fixed volume flow flux and static pressure are respectively applied. The outlet static pressure is changed to adjust the operating cavitation number. The rotational and static domains are coupled using the ALE (Arbitrary Lagrangian-Eulerian) method. The time step for unsteady simulations Δt is set at 1/1440 of the impeller rotational duration, i.e., $\Delta t \cong 2.60\times10^{-5}$s, which has been determined after the dependence check. Firstly, the computations are conducted for the flow rate of Q/Q_{d} =1.0, 0.8, 0.6, 0.4, 0.2 without cavitation to verify the numerical model in terms of the hydraulic performance. Then, we carry out the cavitation analysis using MP model for the three flow rate conditions, Q/Q_{d} =1.0, 0.6, 0.2 subsequently. Table 2 summarizes the parameter settings of MP model. In the CFD analysis, the pump heads are calculated by the difference of mass-averaged total pressure between the inlet and outlet boundaries. Thrusts and torque are calculated by the surface integration of the pressure and shear stress acting on the wall of rotating components, i.e., the impeller, the balancing drum, and the shaft.

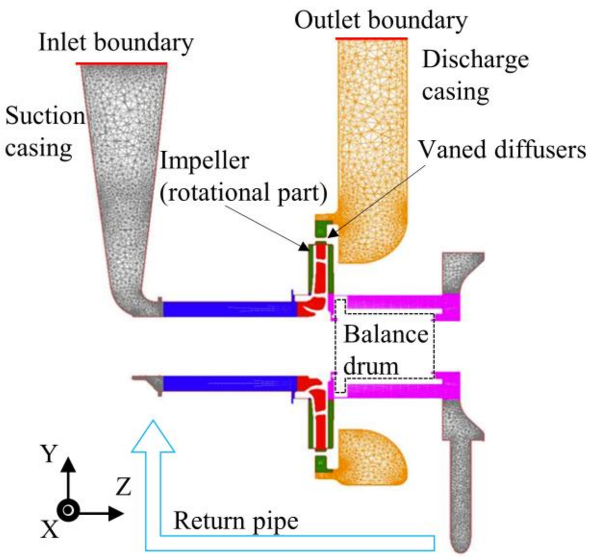

Fig. 2 Sectional view of the computation domain

Table 2 Parameters of MP model

Fluid	Compressible flow
Number of nuclei [m^{-3}]	1×10^{8}
Radius of nuclei, R_{c} [m]	0.0002
Expansion coefficient, C_{e}	0.50
Shrinkage coefficient, C_{s}	0.25

[DOI: 10.1299/jfst.2024jfst0011]
© 2024 The Japan Society of Mechanical Engineers

2.4 Experimental method

For the validation of the present numerical simulation, we conduct the experiment of the target pump. Figure 3 shows a layout of the test loop used in this study. The test loop is a closed system filled with water and consists of a tank, piping and the test pump. The top of the tank is directly connected to a vacuum pump and a compressor. The pressure in the loop is controlled by changing the pressure of the air above the liquid surface in the tank. A valve installed at a discharge pipe is used to adjust the discharge flow rate. An electromagnetic flowmeter installed downstream of the test pump is used to measure the discharge flow rate. The balancing flow rate is measured by an ultrasonic flowmeter installed at the middle of the return pipe. The total head rise of the pump is calculated from the difference between outlet and inlet static pressures, P_{out} and P_{in}, measured by a differential pressure transducer with considering the dynamic pressure based on the area-averaged flow velocity at the corresponding locations. The shaft torque T is measured by a torque meter installed between the pump shaft and the motor shaft, and the mechanical loss T_0 estimated by the measurement is subtracted from the measured torque T. The axial thrust F_{A} on the rotor system is measured by three load cells installed on both axial sides of the thrust bearing. The axial thrust measured by this method is the residual axial thrust as a sum of all axial forces acting on the rotor system. In order to investigate the mechanism of the axial thrust, the test pump has prepared the static pressure taps at several radial locations in the impeller back side gap and in the balance room. In this study, the thrust acting on the balance drum $F_{\mathrm{A,BD}}$ is estimated assuming that the side gap pressure in the proximity of the inlet of the balance channel P_{SG} and the balance room pressure P_{BR} uniformly act the upstream and downstream surfaces of the balance drum respectively (Fig. 4). The thrust acting on the impeller $F_{\mathrm{A,IM}}$ can be calculated from the difference between F_{A} and $F_{\mathrm{A,BD}}$.

$$F_{\mathrm{A,BD}} = A_{\mathrm{BD}}(P_{\mathrm{SG}} - P_{\mathrm{BR}}) \tag{11}$$
$$F_{\mathrm{A,IM}} = F_{\mathrm{A}} - F_{\mathrm{A,BD}} \tag{12}$$

where A_{BD} is the axial projection area of the balance drum. Since the actual pressure distributions of the drum may not be uniform, this method is used to qualitatively evaluate the trend of the axial forces against the occurrence of cavitation. The pump performance is summarized in the non-dimensional form using the cavitation number σ, the head coefficient ψ, the shaft power coefficient τ, the efficiency η, the axial thrust coefficient C_{FA} and static pressure coefficient ψ_{s}, which are defined as follows;

$$\sigma = \frac{P_{\mathrm{in}} - P_{\mathrm{v}}}{\rho_{\mathrm{L}} U_1^2/2}, \psi = \frac{gH}{U_2^2}, \tau = \frac{\omega(T - T_0)}{\rho_{\mathrm{L}} A_{\mathrm{out}} U_2^3}, \eta = \frac{\rho_{\mathrm{L}} gQH}{\omega(T - T_0)}, C_{\mathrm{FA}} = \frac{2F_{\mathrm{A}}}{\rho_{\mathrm{L}} A_{\mathrm{out}} U_2^3}, \psi_{\mathrm{s}} = \frac{P_{\mathrm{s}}}{\rho_{\mathrm{L}} U_2^2} \tag{13}$$

where P_{v} is the saturated vapor pressure, g is the gravitational acceleration, U_1 is the impeller rotating velocity at the inlet tip, U_2 is the impeller rotating velocity at the outlet, ω is the angular speed of impeller (=$2\pi N/60$), H is the total head of pump, A_{out} is the area of impeller outlet and P_{s} is the static pressure difference from that at the inlet of impeller.

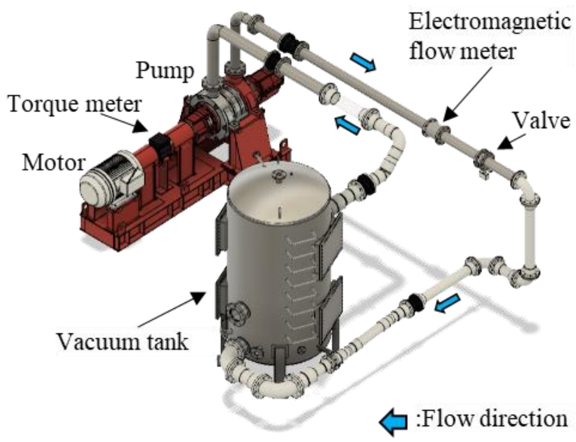

Fig. 3 Test cavitation loop used in this study. The suction pressure condition can be changed by adjusting the pressure inside the vacuum tank using a vacuum pump.

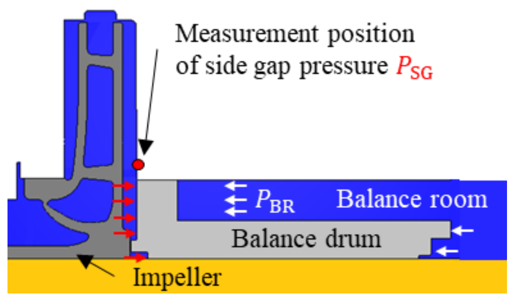

Fig. 4 Estimation method of axial thrust force generated by the balance drum

[DOI: 10.1299/jfst.2024jfst0011]
© 2024 The Japan Society of Mechanical Engineers

Note that the elevation of the suction pipeline of the loop is higher than the inlet of the pump. The pressure there falls below the saturated vapor pressure and a gas phase appears before the head breakdown in conditions of low flow rate. This constrains the lower limit of experimental range of σ at low flow rates.

2.5 Visualization method

An overview of the visualization method used in this study is shown in Fig. 5. The pipe connected to the inlet of impeller is made of transparent acrylic resin for visualization. Since it is difficult to observe the impeller located inside the pump from the outer circumference of the pipe directly, two acrylic prisms are attached on the outer circumference of the pipe. The shape and layout of the prisms have been designed to take account of the refraction between the water and acrylic resin so that the blade surface inside the pump can be observed through them. Two prism windows are provided symmetrically on the both sides, one for the observation and the other for the lighting. This method does not require the insertion of an observation device and enables noninvasive observation of the flow. However, it should be noted that images obtained are to be slightly distorted due to the difference in refractive index between water and acrylic resin. In this study, a high-speed camera is used to observe cavitation. To reduce blurring of the unsteady cavity behavior as much as possible, the shutter speed and the frame rate are set at 10 μs and 10000 fps, respectively. A fiber-scope type LED light is used for the lighting.

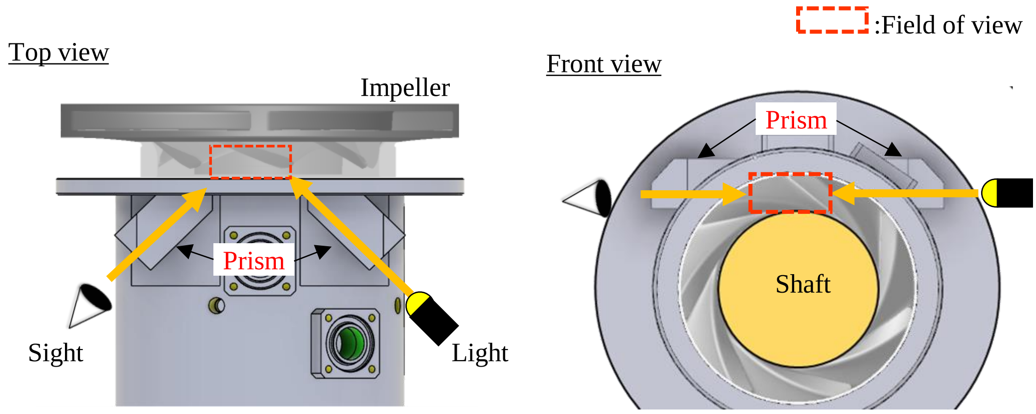

Fig. 5 Visualization method with acrylic pipe. Two prisms, one for the camera and another for the lighting, are attached to enable the noninvasive observation.

3 Results and discussion

3.1 Performance characteristics without cavitation

First, the computed and measured pump performances without cavitation are compared. Figure 6 shows the pump performance. The error bar presented for the experimental results means the twice of the standard deviation of ten

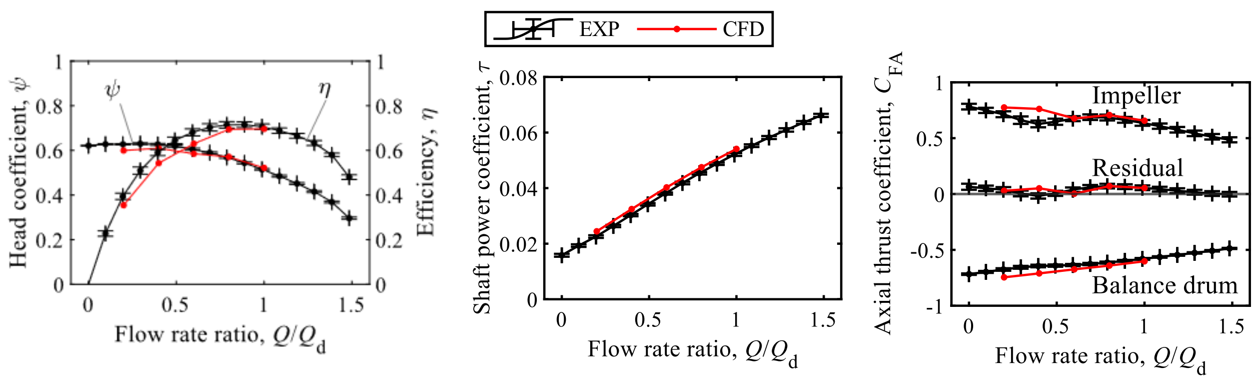

(a) Pump performance (b) Shaft power coefficient (c) Axial thrust

Fig. 6 Performance characteristics without cavitation. Present numerical simulation well reproduces the hydraulic performances as well as the residual and decomposed axial thrust acting on the rotor system.

[DOI: 10.1299/jfst.2024jfst0011]
© 2024 The Japan Society of Mechanical Engineers

measured samples. It is seen that the computed head and efficiency agree well with the measured ones at Q/Q_{d} =1.0 and 0.8 (Fig. 6 (a)). On the other hand, discrepancies are observed at the lower flow rates. Since the shaft power is well matched between experiments and analysis over all the flow rates (Fig. 6 (b)), it is concluded that the head is underestimated at the partial flow rates in the present CFD simulations. However, the maximum error is as small as 5% or less. Secondly, Fig. 6 (c) shows the axial thrust characteristics. The trends of not only the residuals but also the respective values decomposed into the impeller and the balance drum are in good agreement between the present simulations and the experiments. From the above, it is confirmed that the prediction accuracy is sufficient for no-cavitation conditions. On the basis of the above, the results of cavitation analysis will be presented and then discussed from the next section.

3.2 Performance characteristics under cavitation

As a part of the accuracy verification of the MP model, RANS simulations using MP model as well as a typical one-equation model, FC model (Singhal et al., 2002), were carried out at the design flow rate (Q/Q_{d} =1.0). The results have been compared between the two models as well as with the experiments, and it is found that the difference of the two simulations is small enough, indicating that the accuracy of MP model prediction is sufficient. The details of FC model are described in Appendix.

The prediction and measured pump performances under cavitation are shown in Fig. 7. At the partial flow rates of Q/Q_{d} =0.6 and 0.2, both the experiment and simulation could not be conducted up to the point of low cavitation number with head degradation; in the experiment, the two-phase flow occurs at the moderate cavitation number before the head

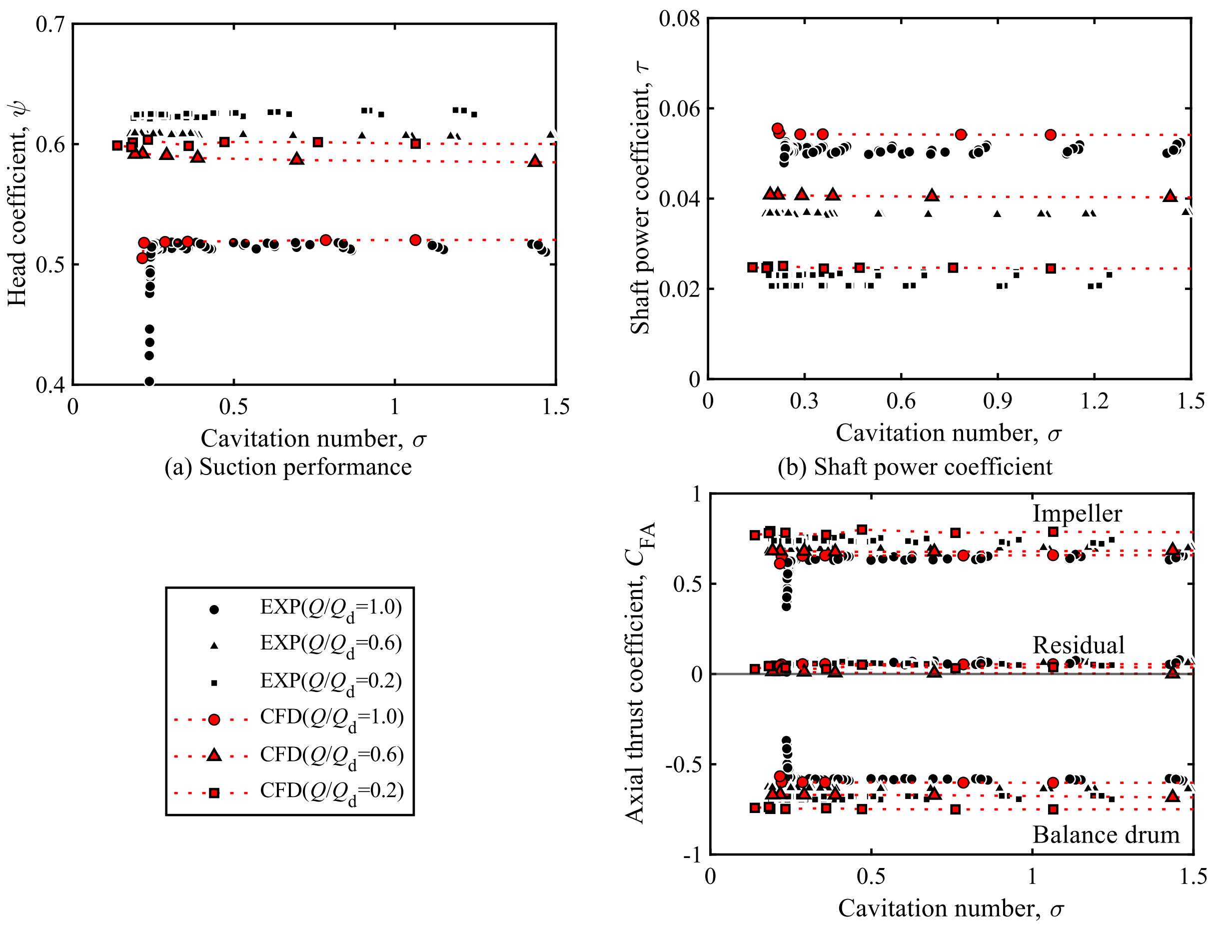

(a) Suction performance

(b) Shaft power coefficient

(c) Axial thrust coefficient

Fig. 7 Performance characteristics under cavitation. Present numerical simulation well reproduces the head breakdown curve as similar to the experiment at the design flow rate. The shaft power coefficient is almost constant even after the head reduction both in the simulation and in the experiment. Thus, the head reduction of this pump at the design flow rate is mainly due to an increase of a pressure loss caused by the cavity growth. The thrust of the rotor system has dropped as well as the thrust of acting on the impeller and balance drum has decreased at the same time as the head drop.

[DOI: 10.1299/jfst.2024jfst0011]
© 2024 The Japan Society of Mechanical Engineers

breakdown due to the high elevation of the suction pipeline as explained above, while the numerical simulation cannot be conducted due to some convergence problem in the head breakdown process. Before the breakdown, a certain cavitation instability occurs, which will be reported in our future study after the detailed analysis. Therefore, the discussion on the head breakdown is herein made only at Q/Q_{d} =1.0. Firstly, a good agreement of the head breakdown curve is found between the experiment and the simulation; the head is almost kept constant at high cavitation numbers before the head breakdown, then decreases sharply at the similar cavitation number. A detailed discussion of the head degradation is given in the next section with a comparison of cavitation structure. Next, the shaft power coefficient τ is checked. Both the simulation and the experiment show a slight increase immediately after the beginning of the head reduction. However, it is very small (only about 2% of the non-cavitating shaft power), and therefore the Euler head has not changed significantly, and the head reduction of this pump at the design flow rate starts mainly due to an increase of a pressure loss caused by the cavity growth. Figure 7 (c) shows the axial thrust characteristics, and the thrust of the rotor system decreases at the same time as the head drop both in the simulation and in the experiment. Furthermore, the thrusts acting on the impeller and balance drum are found to decrease as well. For the detailed discussion, the pressure distributions at radial position r in the front and back side gaps of the impeller are shown in Fig. 8. The radial position is nondimensionalized by the impeller radius R_2. It should be noted that the radial position of $r/R_2 \approx 0.5$ on the front side is that of leakage flow path at the liner ring gap where the pressure decreases largely due to the skin friction loss of leakage flow. The region with lower r/R_2 ($0.3 < r/R_2 < 0.5$) on the front side is the inlet region of impeller. The pressures are circumferentially-averaged ones shown as the difference from the static pressure at the impeller inlet. From the non-cavitation state (σ = 4.25) to just before the head drop (σ = 0.22), there is no difference in the pressure distribution. The aforementioned small change in the Euler head suggests that the angular momentum brought into the impeller side gap is not significantly different before and after the head drop. Therefore, the pressure gradient is expected to change hardly even after the head is reduced at least at the early stage of reduction. However, the pressures inside the front and back side gaps both decrease uniformly due to the head reduction. Therefore, the pressure difference between the front and back sides of the impeller inside the inlet radius ($r/R_2 \leq 0.5$) becomes smaller. Then it is found that the decreasing thrust area of the impeller due to cavitation is simply caused by the decrease in the impeller outlet static pressure, i.e., the reduction of the impeller head.

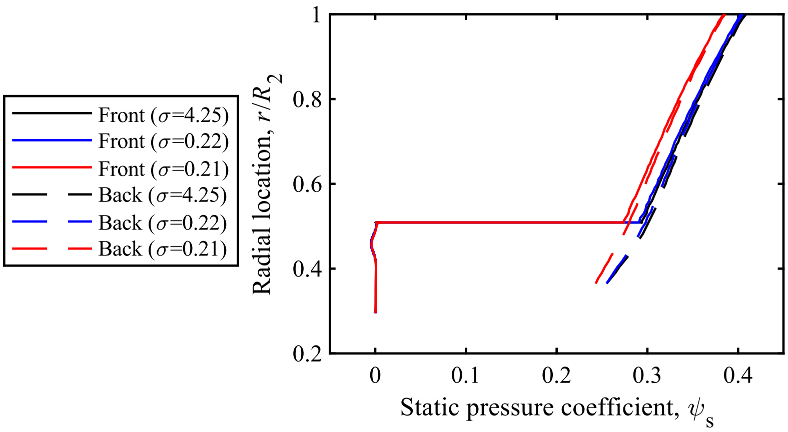

Fig. 8 Pressure distribution of impeller shroud wall. Pressure coefficient is defined as a circumferentially averaged local pressure minus area averaged inlet static pressure normalized by the dynamic pressure based on the impeller outlet velocity. The figure indicates that the slope of pressure coefficient in the front and back side gaps are not changed while the level of the pressure coefficient is decreased against the decrease of the cavitation number, which causes the decrease of the impeller axial thrust due to cavity growth.

3.3 Cavity structure

Figure 9 shows the cavity structure observed from the right window at the design flow rate. Each simulation result shows an isosurface of α=0.1 for the instantaneous void fraction, while the experimental one shows a typical instantaneous image. As a result, the simulation well predicts the location and areas of the cavity. The observed view in the experiment cannot capture the trailing edge of the cavity because it is shaded by the neighbor blade. Therefore, the

 © 2024 The Japan Society of Mechanical Engineers

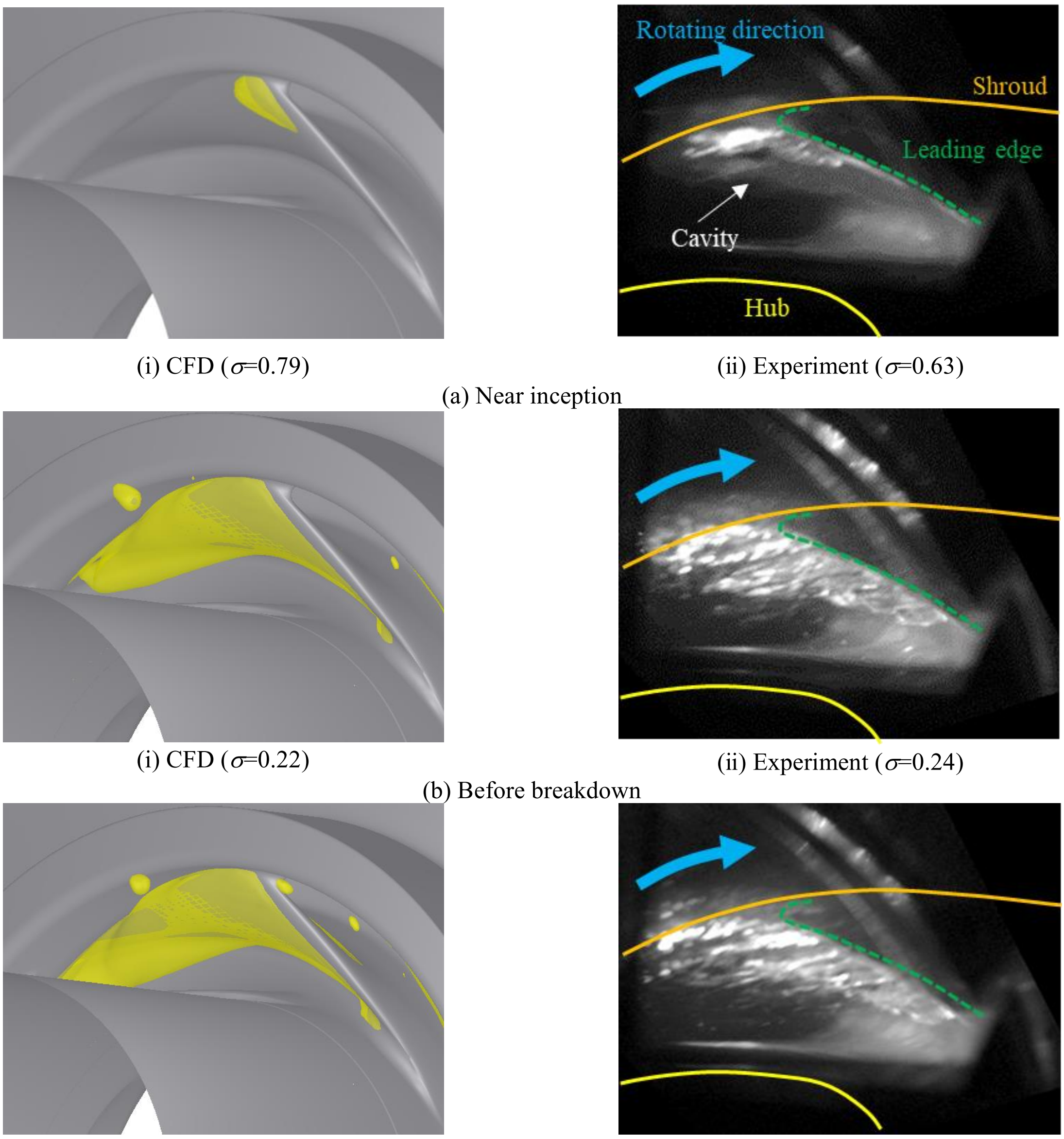

(i) CFD (σ=0.79) (ii) Experiment (σ=0.63)

(a) Near inception

(i) CFD (σ=0.22) (ii) Experiment (σ=0.24)

(b) Before breakdown

(i) CFD (σ=0.21) (ii) Experiment (σ=0.23)

(c) After breakdown

Fig. 9 Cavitation pattern (Q/Q_d =1.0) at a certain instant. The development of cavitation looks similar between the present numerical simulation and the experiment. The trailing edge of cavitation gets into the blade passage, which seems to resulting in the sharp head drop at (c).

difference in the cavity structure before and after the head drop cannot be well recognized. It has been reported by Medvitz et al. (2002) and Nohmi et al. (2003) that the head of a centrifugal pump decreases when the cavitating region extends up to the throat of the impeller channel. In order to investigate the cause of the head drop, the void fraction distributions in the impeller obtained by the numerical simulation are utilized here. Distributions of void fraction in the cross section at each 0.2 pitch in one pitch of the blade are shown in Fig. 10. It can be seen that the cavities grow on the pressure side just after the head reduction. It is also found that the growing cavities are attached to the shroud wall and they seem to block the flow passage. Therefore, the main cause of the sharp head drop is the cavitation on the pressure surface of blades as a result of the extension of suction surface cavitation into the throat position. On the basis of the above consideration, it is concluded that the simulation is valid at Q/Q_d =1.0.

Next, cavity structures at the partial flow rate conditions are shown in Figs. 11 and 12. Since the head degradation could not be achieved at these conditions as explained above, the comparisons between the simulation and the experiment are made near the cavitation inception and at low σ. At Q/Q_d =0.6, the position of inception locates at a tip of blade, which is not very different from the design point (Fig. 11 (a)). However, the cavity pattern is quite different at low σ. It

[DOI: 10.1299/jfst.2024jfst0011]
© 2024 The Japan Society of Mechanical Engineers

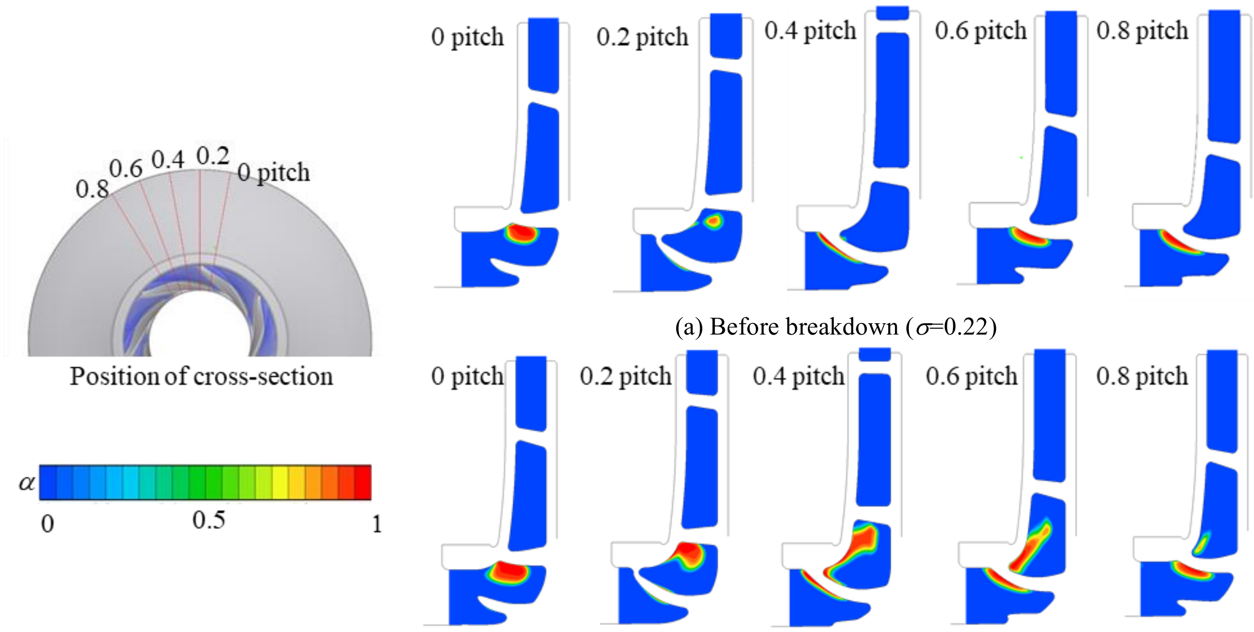

Fig.10 Void fraction distributions obtained by the numerical simulation before and after the head breakdown. Significant development of cavitation at the corner between pressure and shroud surfaces can been seen just after the head breakdown.

can be seen that the grown cavities are detached from the blade surface and do not yet get into the channel in both the experiment and the numerical simulation (Fig. 11 (b)), probably due to the development of the recirculation zone at the inlet tip of impeller. Thus, in this flow rate, the cavity structure is approximately predictable by the present numerical simulation. On the other hand, the experimental and simulation results do not well match at further low flow rate Q/Q_{d} =0.2, as can be seen in Fig. 12. In the experiment, a tip separation vortex cavitation is mainly observed (Fig. 12 (a)), and the cavities caused in the vortices upstream of the impeller clearly appear in the lower pressure condition (Fig. 12 (b)). However, the numerical simulation does not reproduce such vortex cavities. This difference is probably due to the fact that the mesh used in this study is insufficient for resolving the vortex cavities apart from the blade surfaces. In addition, RANS simulations have generally the difficulty in predicting local eddy structures with unsteadiness. From the above, the cavity prediction at low flow rate (Q/Q_{d} =0.2) requires further validation in terms of the physical model and the grid resolution.

Finally, one of the characteristics of MP model is described, that is the capability of simulating the bubble state of cavitation in each computational cell. Figure 13 shows the distributions of i-th moment variable at the same cross-section, 0.4 pitch, at the cavitation number just after the head breakdown. It is possible to obtain such detailed data on states of bubbles as well as void fraction. Note that M_3 should have a distribution similar to that of α, as can be understood through Eq. (8). For the bubble number density M_0, it can be seen that the distribution is different from that of the void fraction (Fig.10 and Fig.13 (a)). To reveal the representation performance of polydispersity by MP model, we define the index of polydispersity I_{p} as follows, and it is plotted in Fig. 13 (e);

$$I_{\mathrm{p}} = \left| \log_{10} \frac{M_3/M_2}{(M_3/M_0)^{\frac{1}{3}}} \right| \tag{14}$$

I_{p} is defined as the Sauter mean diameter divided by the volume mean diameter. This variable should be 0 for monodisperse and the greater value means the significance of polydispersity. It is seen that I_{p} takes large value at the surface of the cavitation region, indicating that the MP model can simulate the polydispersity of cavitation flow. Although the validation of such bubble states has not yet been conducted unfortunately due to the insufficient image quality of experimental observation, this kind of information may be useful for more physical analysis on cavitation related phenomena such as incipient cavitation structure, cavitation erosion in the near future.

[DOI: 10.1299/jfst.2024jfst0011]
© 2024 The Japan Society of Mechanical Engineers

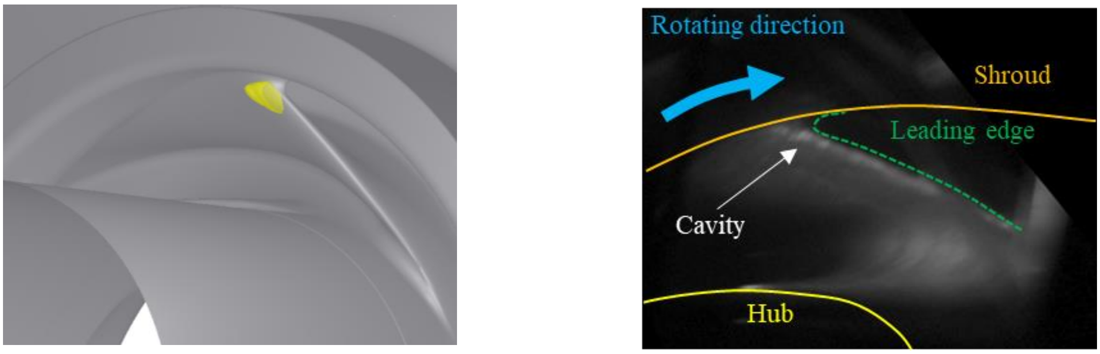

(i) CFD (σ=0.71) (ii) Experiment (σ=1.03)

(a) Near inception

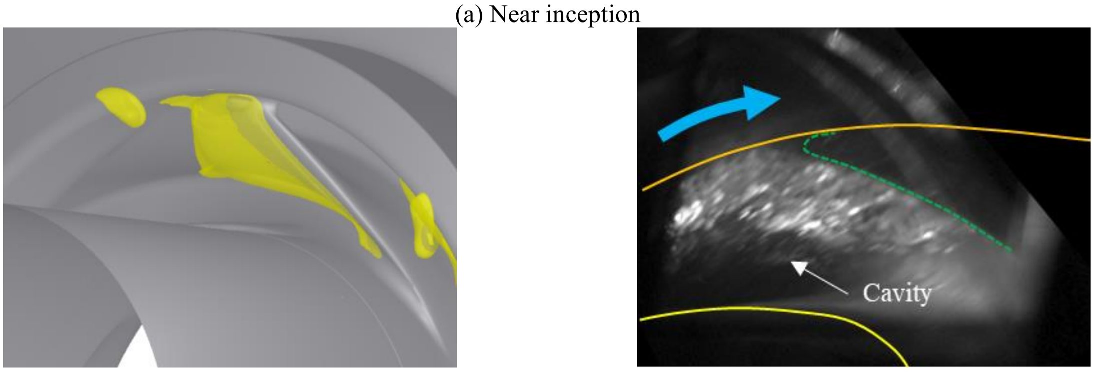

(i) CFD (σ=0.21) (ii) Experiment (σ=0.20)

(b) Low σ

Fig.11 Cavitation pattern (Q/Q_{d} =0.6). The inception location is almost the same; at a tip of blade, as the design point. At low σ, the grown cavities are detached from the blade surface and do not get into the channel. The main cause of structure of cavitation is probably the recirculation zone at the inlet tip of impeller. The analysis qualitatively predicts these behaviors of the cavity.

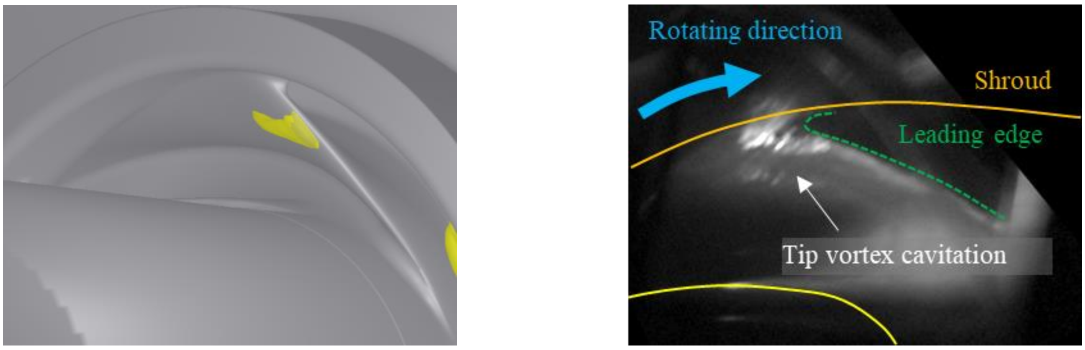

(i) CFD (σ=0.36) (ii) Experiment (σ=0.43)

(a) Near inception

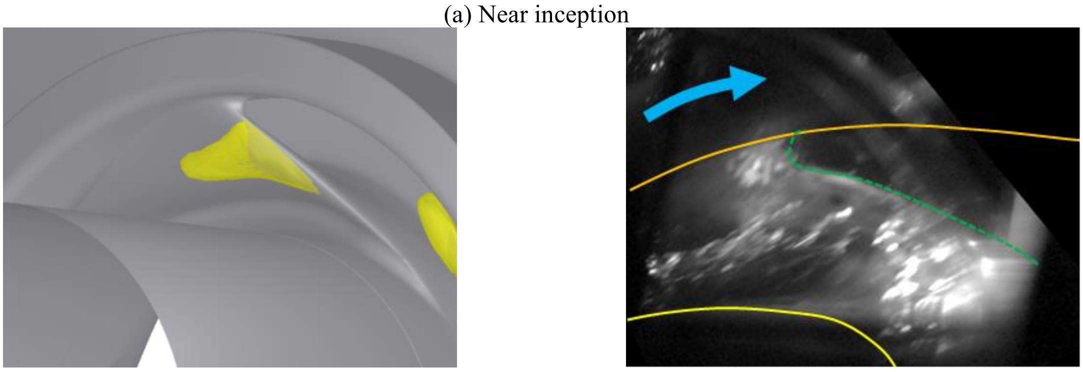

(i) CFD (σ=0.18) (ii) Experiment (σ=0.21)

(b) Low σ

Fig.12 Cavitation pattern (Q/Q_{d} =0.2). The analysis cannot predict the cavitation pattern accurately from the inception. The tip separation vortex cavitation observed in experiments is not reproduced in the analysis. The difference between the experimental and analytical results is more apparent under low σ.

[DOI: 10.1299/jfst.2024jfst0011]
© 2024 The Japan Society of Mechanical Engineers

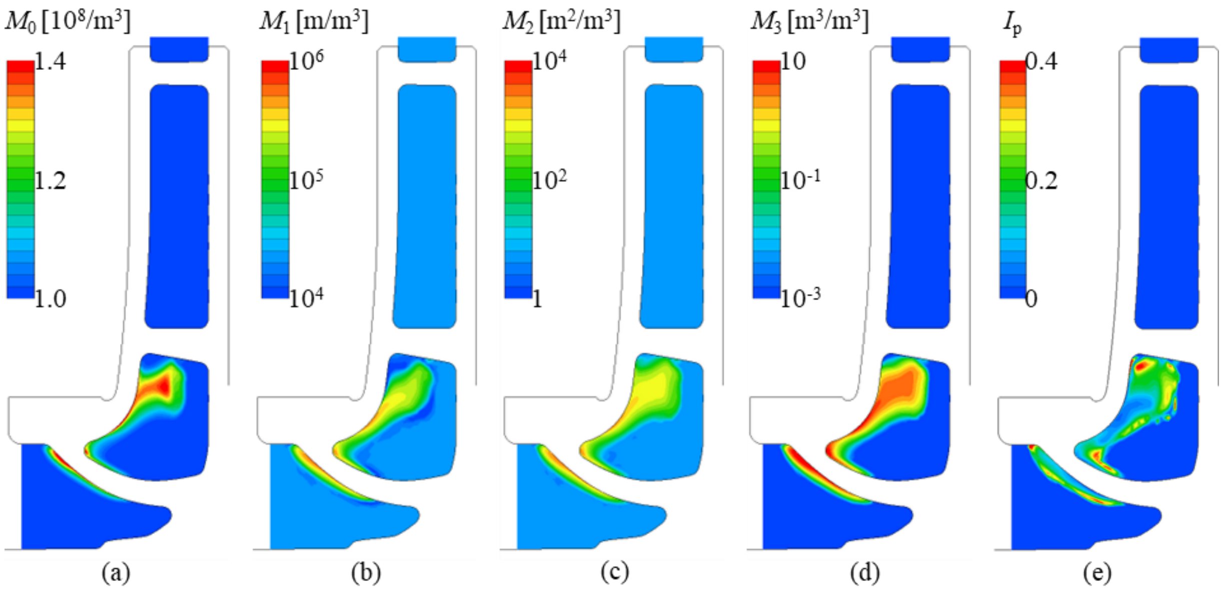

Fig. 13 Bubble state for MP model at 0.4 pitch (σ=0.21), (a) Bubble number density, (b) Bubble radius density, (c) Bubble surface density, (d) Bubble volume density, (e) Index of polydispersity. The distribution of the bubble number density M_0 is different from that of the void fraction and other variables M_i. The larger the index of polydispersity I_p is, the more significant the polydispersity. It takes large value at the surface of the cavitation region, indicating that the MP model can simulate the polydispersity of cavitation flow.

4. Conclusion

In this study, unsteady RANS simulation using MP model was carried out for the final stage model of a three-stage centrifugal pump. The experiment was also conducted to obtain the head breakdown characteristics, the trend of the axial thrust force against the cavity development as well as the visualized cavitation images for the validation of the numerical simulation. Through the detailed comparisons between the simulation and the experiment, the following conclusions were obtained.

(1) Multi-Process model could predict the cavitation performance of the target pump at the design flow rate. Furthermore, the shaft power and thrust characteristics under cavitation were also well predicted.

(2) At design flow rate, the numerical simulation suggests that the head breakdown of the pump is mainly led by the increase of the pressure loss. The development of cavitation at the corner between the pressure and shroud surfaces of the throat channel along with the extension of the sheet cavity into the throat of blade passage enhances the flow blockage, which seems to result in the increase of the pressure loss. This head drop causes a decrease in the axial thrust of the impeller and the thrust of the balance drum. As a result, the thrust of the entire rotor system is decreased.

(3) The predicted cavity appearance also qualitatively agreed with the experimental observation during the head breakdown processes at the design flow rate of Q/Q_d=1.0, which supports the agreement of the hydraulic performance degradation and the axial thrust characteristics. Similarly, the qualitative agreement of cavity appearance was observed at Q/Q_d =0.6. However, there were noticeable differences at a deep low flow rate of Q/Q_d =0.2; from experimental observation, some portion of cavitation was found be formed in the vortical flows which could not be reproduced by the present numerical simulation. This disagreement is thought to be due to the insufficient grid resolution with RANS based simulation.

(4) MP model can clearly express the polydispersity of cavitation flow. Although it needs further experimental validation, this information of bubble states may be useful for obtaining a deeper insight on cavitation phenomenon.

Acknowledgement

Some part of this study has been carried out under the activity of WG2 in High-Precision Prediction of fluid performance and innovative fluid design Research Committee of Turbomachinery Society of Japan. Also, the present study was supported to modify the solution setup by Dr. Takahito Miki (Hexagon). We greatly appreciate his contribution.

[DOI: 10.1299/jfst.2024jfst0011] © 2024 The Japan Society of Mechanical Engineers

Appendix

Comparison with Full Cavitation model

A typical one-equation model chosen here for the comparison with MP Model was so-called Full Cavitation (FC) model developed by Singhal et al. (2015), which has been implemented in the current solver, scFLOW. Table 3 summarizes the setting of the parameters in FC model, which are the default values given in the original paper. For more details of the model, see the original paper.

Figure 14 shows a comparison of suction performance between the two models, MP and FC models. In the both two models, the head is kept almost constant before the head breakdown, then drops sharply with the decrease of cavitation number σ. However, FC model tends to show a slightly gradual drop of the head, while MP model is able to predict the sudden head drop as similar to the experiment. Because of the parameter dependence especially for FC model, we do not conclude here which model is superior. It is just confirmed that MP model can predict suction performance at least with the same level of accuracy as typical one-equation models.

Table 3 Parameters of FC model

Surface tension, γ [N/m]	0.07275
Mass fraction of noncondensable gas, Y_g	1.0×10^{-6}
Coefficient for evaporation, C_e	0.02
Coefficient for condensation, C_c	0.01

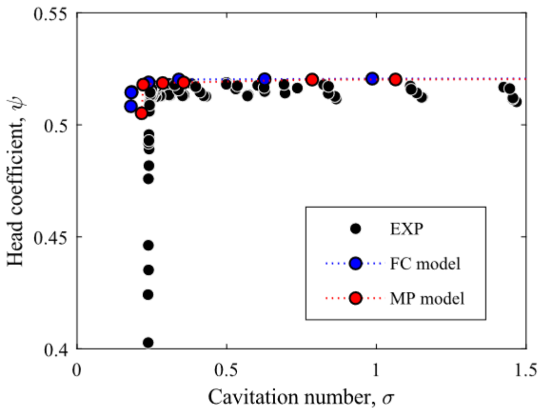

Fig. 14 Comparison of the head breakdown curve at the design flow rate. Both MP and FC models well simulate the head breakdown curve.

References

Coutier-Delgosha, O., Reboud, J. L. and Delannoy, Y., Numerical simulation of the unsteady behaviour of cavitating flows, International Journal for Numerical Methods in Fluids, Vol. 42, Issue 5 (2003), pp. 527-548.

Karakas, E. S., Tokgöz, N., Watanabe, H., Aureli, M. and Evrensel, C. A., Comparison of transport equation-based cavitation models and application to industrial pumps with inducers, ASME. Journal of Fluids Engineering, Vol. 144, Issue 1 (2022), 011201, DOI:10.1115/1.4051471.

Medvitz, R. B., Kunz, R. F., Boger, D. A., Lindau, J. W., Yocum, A. M. and Pauley, L. L., Performance analysis of cavitating flow in centrifugal pumps using multiphase CFD, ASME. Journal of Fluids Engineering, Vol.124, Issue 2 (2002), pp.377-383.

Miki, T., Fujiyama, K., Tsuda, S. and Irie, T., Cavitation analysis of a Delft twisted hydrofoil using multi-process cavitation model, Journal of Physics: Conference Series, Vol. 1909 (2021), 012014, DOI:10.1088/1742-6596/1909/1/012014.

Miyabe, M. and Maeda, H., Numerical prediction of pump performance drop and erosion area due to cavitation in a double-suction centrifugal feed pump, Proceedings of the ASME-JSME-KSME 2011 Joint Fluids Engineering Conference, Vol. 1, Symposia - Parts A, B, C and D (2011), pp.121-128.

Nohmi, M., Goto, A., Iga, Y. and Ikohagi, T., Experimental and numerical study of cavitation breakdown in a centrifugal pump, Proceedings of the ASME/JSME 2003 4th Joint Fluids Summer Engineering Conference, Vol. 1, Fora - Parts A, B, C and D (2003), pp.1251-1258.

Nohmi, M., Ikohagi T. and Iga, Y., Numerical prediction method of cavitation erosion, Proceedings of the ASME 2008 Fluids Engineering Division Summer Meeting collocated with the Heat Transfer, Energy Sustainability, and 3rd

[DOI: 10.1299/jfst.2024jfst0011]
© 2024 The Japan Society of Mechanical Engineers

Energy Nanotechnology Conference, Vol.1, Symposia - Parts A and B (2009), pp. 1139-1145.
Randolph, D. A. and Larson, A. M., Theory of Particulate Processes, (1971), Academic Press.
Saito Y., Nakamori I. and Ikohagi T., Numerical analysis of unsteady vaporous cavitating flow around a hydrofoil, Proceedings of 5th International Symposium on cavitation (2003), Paper No. OS-3-003.
Schnerr, G. H. and Sauer, J., Physical and numerical modeling of unsteady cavitation dynamics, Proceedings of 4th International Conference on Multiphase Flow (2001).
Singhal, A.K., Athavale, M. M., Li, H. and Jiang, Y., Mathematical basis and validation of the full cavitation model, ASME. Journal of Fluids Engineering, Vol. 124, Issue3 (2002), pp.617-624.
Sun, W. and Tan, L., Cavitation-vortex-pressure fluctuation interaction in a centrifugal pump using bubble rotation modified cavitation model under partial load, ASME. Journal of Fluids Engineering. Vol.142, Issue 5 (2020), 051206, DOI:10.1115/1.4045615.
Takamine, T., Furukawa, D., Watanabe, S., Watanabe, H. and Miyagawa, K., Experimental analysis of diffuser rotating stall in a three-stage centrifugal pump, International Journal of Fluid Machinery and Systems, Vol. 11 (2018), pp.77-84.
Takamine, T., Nakano, S., Watanabe, S. and Watanabe, H., Influence of axial rotor offset on residual axial thrust characteristics of a centrifugal pump at low flow rates, International Journal of Fluid Machinery and Systems, Vol. 13 (2020), pp.655-667.
Tsuda, S. and Watanabe, S., Application of multi-process cavitation model for cavitating flow in cold water and in liquid nitrogen around a hydrofoil, Proceedings of the ASME/JSME/KSME 2015 Joint Fluids Engineering Conference, Vol. 2A, Fora - Part 2 (2015), DOI:10.1115/AJKFluids2015-05532.
Wang, Y., Effects of nuclei size distribution on the dynamics of a spherical cloud of cavitation bubbles, ASME. Journal of Fluids Engineering, Vol.121, No.4 (1999), pp.881-886.
Zwart, P. J., Gerber, A. G. and Belamri, T., A two-phase flow model for predicting cavitation dynamics, Proceedings of 5th International Conference on Multiphase Flow (2004), Paper No. 152.

[DOI: 10.1299/jfst.2024jfst0011]
© 2024 The Japan Society of Mechanical Engineers